

Grappling claws for a robot to climb rough wall surfaces: Mechanical design, grasping algorithm, and experiments

Fengyu Xu^{a,*}, Fanchang Meng^a, Quansheng Jiang^b, Gaoliang Peng^c

^a College of Automation, Nanjing University of Posts and Telecommunications and Jiangsu Engineering Lab for IOT Intelligent Robots (IOTRobot), Nanjing, 210023, China

^b School of Mechanical Engineer, Suzhou University of Science and Technology, Suzhou, 215009, China

^c School of Mechanics and Electronics, Harbin Institute of Technology, Harbin, 150001, China

ARTICLE INFO

Article history:

Received 24 December 2018

Received in revised form 24 April 2019

Accepted 10 March 2020

Available online 13 March 2020

Keywords:

Flexible grasping claw

Grasping discrimination algorithm

3D wall

Asperity of rough wall surfaces

ABSTRACT

Wall-climbing robots have been widely applied in the inspection of smooth walls. However, only a few adhesion methods have been developed for robots that will allow them to climb cliffs and dusty, high-altitude, rough walls (constructed using coarse concrete, bricks, and stones, etc.) that may be subjected to vibrations. This paper proposes a suitable adhesion method that employs grappling-hook-like claws arranged in a cross shape. First, we address the implementation mechanism required. Then, a method of extracting the characteristic parameter is revealed rough wall was devised, 3D profiles of rough walls were simulated, and the discriminant conditions necessary for the claws to stably grasp the wall were provided. A method of triangulation is proposed to judge which regions of a 3D wall can be gripped, and we subsequently present a grasping discrimination algorithm for the interaction between the miniature claws and 3D wall profile. Finally, a prototype of the grappling-hook-like claw system was fabricated. A test platform was built to test the robot which incorporates an electromagnetic vibration shaker to simulate a vibrating wall. Experiments were then carried out on the robot using the vibrating wall and a random outdoor wall. The results verified the feasibility of the proposed claws and the validity of the discriminant algorithm for gripping 3D walls. Compared with traditional adhesion approaches, the proposed method (based on hook-like claws) is more adaptable to suit various types of wall. It also has higher resistance to disturbances and so provides a more reliable method of adhesion for robots on rough walls.

© 2020 Elsevier B.V. All rights reserved.

1. Introduction

In order to ensure the safety of special buildings, e.g. cable-stayed bridge towers, the walls of nuclear reactors, and viaducts in remote mountain areas, it is necessary to conduct regular inspections. However, manual inspection of their status is characterized by a long cycle of difficult and risky inspections. Hence, it is highly desirable that specialized and automated inspection robots can be developed.

1.1. Background and significance

The surfaces of high-altitude buildings constructed using stone, concrete, and rough bricks generally show signs of serious ash deposition and are often continually subjected to vibration owing to passing vehicles and high-altitude wind loads. The inertial forces acting on these kinds of wall surfaces greatly affect

the stability of climbing robots. This means that more stringent requirements are placed on the adhesion methods used by the wall-climbing robots employed. Traditional magnetic methods are extensively used to inspect magnetic walls [1,2]. Vacuum suction (adhesion due to negative pressure) methods can be adapted to different walls [3,4], but are essentially limited to the inspection of smooth walls. Methods employing vibrating suckers [5], highly-efficient negative-pressure suckers with a centrifugal impeller [6], and electrostatic adhesion also have their own scopes of application [7], but do not adapt well to walls that are dusty and have high humidity. Moreover, fractures and random changes in dust and ambient surface temperature of these kinds of wall significantly affect the adhesion efficiency of biomimetic binders which thereby prevents robots climbing such structures.

Scholars have proposed a variety of adhesion methods required for these types of walls. A great deal of important research has been conducted on various aspects of the problems involved, e.g. bionic and other innovative mechanisms to develop various wall-climbing robots (including gecko-inspired climbing

* Corresponding author.

E-mail address: xufengyu598@163.com (F. Xu).

robots, snake-like climbing robots, bionic spider robots, locust-like robots, etc.). To seek improved adhesion modes, scientists have studied the feet of insects and animals with favorable climbing ability using electron microscopes, etc. In the following section, biomimetic climbing robots are briefly introduced from the perspective of bionic dry and moist adhesion, and adhesion with grippers.

1.2. Wall-climbing robots based on bionic dry and moist adhesion methods

With the development of nanotechnology and bionics, scientists have formulated bionic adhesion technology based on the excellent adhesion performance of the feet of animals. Both dry and moist adhesion modes have been devised. As great progress has been made in the technology, various biomimetic climbing robots have been developed, e.g. gecko-inspired robots and spider-like robots, that can climb on smooth surfaces.

A variety of adhesion materials have been developed by Cutkosky et al. to exploit a series of climbing robots, including carbon nanotubes and polymers. Among them, a gecko-inspired climbing robot, 'Stickybot', was developed using dry adhesion technology based on the use of an adhesion agent. The four paws of Stickybot have millions of extremely small adhesive setae. Four tendons on the feet are used for linkage so that the paws can roll outwards and flatten to allow them to easily escape from, and adsorb onto, the surface [8].

Sitti et al. imitated the adhesion mechanism of the paws of geckos according to the van der Waals forces that occur between molecules, and made dry sticky materials using a special process and thus developed several wall-climbing robots [9,10]. Therein, they designed 'Geckobot', a gecko-inspired quadruped climbing robot capable of emulating the walking gait of a gecko (via a linking mechanism) to walk on uneven walls. Moreover, a crawler-type wall-climbing robot was proposed using a caterpillar band made of special dry sticky material so that the robot could stick onto a wall. Moreover, 'Waalbot' is able to move forwards and backwards through the alternate adhesion of three adhesion feet mounted on walking wheels. In this design, Waalbot's paws feature the dry sticky materials.

Daltorio et al. designed a composite climbing robot 'Mini-Whegs' which uses sticky vane wheels [11]. Meanwhile, Menon et al. designed a spider-like climbing robot named 'Abigaille II' which uses silicon resin paws [12,13]. The biological spider robot designed by Vidoni et al. [14], a series of climbing robots proposed by Lee et al. [15], and the biomimetic climbing robot based on a wet adhesion mechanism proposed by He et al. [16], reflect the application of bionic dry and wet adhesion methods to greatly expand the application range of biomimetic adhesion materials.

From the perspective of bionics, Dai et al. investigated the bristle structure, adhesion performance, and motion characteristics of the feet of geckos [17,18]. The viscous materials developed to imitate the paws of geckos were applied to mechanism design to propose a gecko-inspired quadruped robot able to move freely in 3D space and also slopes with an angle of 75°. Wang et al. developed a gecko-inspired robot with feet and flexible components using artificial gecko paws with adhesion materials [19]. They also designed the corresponding gait using flexible links to adapt the movement of the robot. Gao et al. demonstrated biomimetic mechanisms and methods of movement control and thus designed a bionic cockroach robot with a guaranteed level of flexibility [20].

Bionic viscous adhesion, as a kind of advanced adhesion mode, is suitable for smooth walls. However, macromolecular viscous synthetic materials suffer from several defects. For example, processing is often difficult, durability is often poor, and they are prone to the impact of dust on the wall and temperature and humidity of the environment. Thus, they are still in need of further research.

1.3. Wall-climbing robots based on claws

With regard to rough and hard surfaces such as walls, scholars have also studied the properties of the paws of bumblebees, beetles, etc. in order to investigate new adhesion methods that use bionic grippers and to thus develop various bionic robots.

One of the 'RiSE' robots proposed by Spenko et al. uses tiny hooks to allow the robot to cling to a wall. A modular method of combination allowed these to be combined to form a tree-climbing robot with ground walking capability based on 6 modular feet [21]. Goran designed a kind of biomimetic climbing robot, 'DynoClimber' [22], based on biological climbing models which is able to dynamically climb vertical walls with climbing speeds that are significantly faster than previous prototypes. A climbing robot has also been designed by Provancher based on the methods of energy conservation and optimization design [23]. This robot climbs by alternately grasping uplifts on the wall with a pair of mechanical hooks driven by a swinging balancing weight.

By applying a scheme of movement based on peristalsis in worms, Lam designed a tree climbing robot 'Treebot' with compliant claws and also proposed an algorithm for stable motion [24]. The robot created is thus able to grip irregular objects like tree trunks.

Researchers at Stanford University developed a bio-inspired wall-climbing robot, 'Spinybot', whose feet have micro-spines which allow it to climb rough wall surfaces using hooking protuberances [25]. It is suitable for use on rough concrete surfaces and brick walls. Greatly different from conventional wall-climbing robots in terms of adhesion principles, motion mode, and appearance, Spinybot has a strong adaptive capacity to walls.

Sintov developed a claw-inspired wall-climbing robot 'CLIBO' [26]. Like Spinybot, each leg of CLIBO has hooks which enable it to hook onto rough protuberances. Similarly, the rock climbing robot developed by Parness et al. is equipped with grippers fabricated using hundreds of hierarchical arrays of micro-spines [27].

By analyzing the microstructures and surface morphologies of the claws of insects such as bumblebees, Guan et al. also designed bio-inspired claws [28]. The hooks in their claw tips can hook convex and concave points on rough walls and therefore allow a robot to hang on a wall and to climb. By simulating spines and tarsi on the legs of the beetle *Maladera orientalis*, Mei et al. prepared a wall-climbing robot called 'Tbot' [29]. Their robot was equipped with a ratchet wheel on which spines are distributed in an array in the circumferential direction. This wheel serves as the driving wheel allowing the robot to climb upwards on a rough wall. Guan et al. proposed a modular bio-inspired climbing robot with two claws to replace workers engaged in dangerous operations in high-altitude environments [30,31].

To meet the special needs of robot monkeys needing to grasp objects, Cutkosky et al. designed a novel spiny palm densely covered with distributed spines (up to 19 spines per square centimeter) [32]. The robot created can stably grip rough rock surfaces. Kalind presented a micro-spine wheel consisting of multiple compliant spines which can climb rough vertical walls [33]. Using spine arrays, Liu also produced a wall-climbing robot, one that imitates *Serica orientalis* [34]. The feet of this robot have a strong ability to grip which allows it to climb from a vertical wall to a rough ceiling surface.

Using the method of gripping walls with tiny hooks, Xu designed a multi-legged wall-climbing robot with claws and established a mechanical climbing model for it [35–37]. This robot is able to climb static walls but the hooks, unfortunately, are likely to become detached from the wall under large external disturbances (e.g. wind loads and wall vibrations). This is because: (1) the interaction between the hooks and wall does not provide a very effective grip, and (2) the hooks are generally designed

to allow the robot to hang onto the walls and so the interaction between the hooks and walls is merely investigated in 2D.

In summary, wall-climbing robots have been extensively investigated and many successful applications have been achieved. However, in general, the various approaches to adhesion of the robots have their own limited scope of application. In this research, we aim to design a new grappling-hook-like claw and present a discriminating algorithm to allow the claws to grip rough protuberances on 3D walls. We hope the whole claw accomplish the result as the stair climbing robot can balanced perch on the edge of a single step [38].

The rest of the paper is arranged as follows. Section 2 proposes the adhesion method for the grappling claws and extracts the characteristic parameters of rough wall surfaces using a 3D scanner. We also discuss the discriminant conditions for the miniature hooks to stably grip the rough protuberances on walls. In Section 3, we propose a discriminant algorithm for the claws to stably grip the 3D rough walls. A prototype is designed and a test platform for the robot is built as shown in Section 4. Experiments are also carried out to investigate the performance of the robot with respect to gripping the vibrating wall and a random outdoor wall. The conclusions and future research directions are summarized in Section 5.

2. Interaction mechanism between a bionic hook and rough bulge on a wall surface

2.1. Mechanical structure of the grappling-hook-like claws

When designing wall-climbing robots, two key issues need to be taken into account: mobility and adhesivity. In this section, we only pay attention to the method of adhesion acting between the robot and rough wall [35]. On the basis of previously designed claw structures, a grappling-hook-like claw is proposed here that is arranged in the shape of a cross (Fig. 1a–c). Two pairs of secondary claws are fixed on the main structure, each containing an actuating cylinder and multiple elastic hooks. The claws are fixed onto the main structure by various means (including bolts/nuts, elastic steel sheets, spring washers, and connecting plates). The hooks search for convex points that can be gripped onto by slipping on the wall and attach the robot to the rough wall via the grasping force of the claws.

The working principles can be described as follows. The two pairs of secondary claws are symmetrically distributed around the claw module and each secondary claw is connected to a cylinder through a connecting rod. The air pressure in each cylinder is controlled by an external air pump. Inflating (deflating) the cylinder pushes the piston in the cylinder to force the connecting rod outwards (inwards). This drives the slipping of the claws on the wall and realizes grasping and detachment. As the connecting rods move in and out, the hooks in the claw tips can slip on the rough walls allowing them to seek reliable points to grip. When the hooks and rough wall realize a frictional force that is large enough, the elastic steel sheets undergo elastic deformation to allow the contact with the wall to adapt to walls with different levels of uneven roughness.

Fig. 1d illustrates a photograph of the proposed claw gripping a wall. The pair of longitudinal claws play the primary grasping role by gripping the wall using the two upper and lower secondary claws. This not only improves the grasping force, but also enhances the adaptability of the claw system to the wall. The pair of transverse claws are mainly designed to assist gripping and prevent rollover. Arranging the claws in a cross shape enables the robot to attach more stably onto a wall so that it is not susceptible to sideslipping or overturning. These considerations endow the robot with a certain vibration resistance and significantly improve its adaptability to walls.

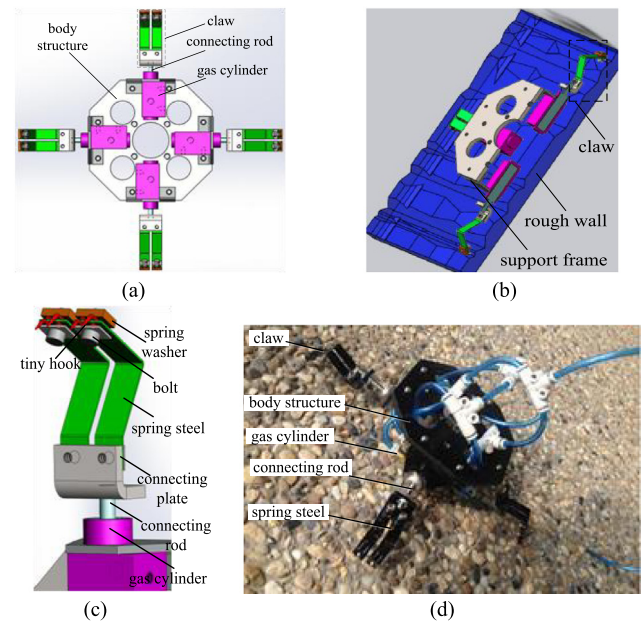


Fig. 1. The structure of the gripper proposed: (a) a 3D model of the grappling gripper, (b) the gripper grasping a wall, (c) the driving module of the gripper, and (d) a photograph of the grappling-hook-like claw in action.

2.2. Method of extracting the characteristic parameters of the rough wall surface

The geometrical shape of a rough surface exerts an important influence on friction, wear, corrosion, lubrication, and other surface characteristics. It is important to characterize the roughness accurately. Rough surface measurement technology can be divided into two categories according to whether the instrument is in contact with the measured object or not. Among them, contact type measuring instruments are more common because of their advantages of high precision, stability, and reliability, but non-contact instruments also confer certain advantages in that they are independent of the hardness of the object under test and can allow non-destructive measurement. This experiment uses a three-dimensional laser scanner, which is based on the principle of optical triangulation, and is a non-contact measurement method. Parameters characterizing the roughness of the wall are critical to the grasp stability of the claws. A 3D scanner was used to scan the wall to extract data so as to characterize the roughness of the wall and allow 2D and 3D profiles of the rough wall to be simulated.

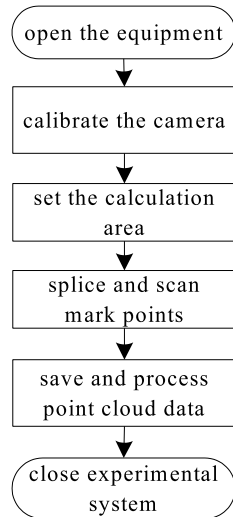
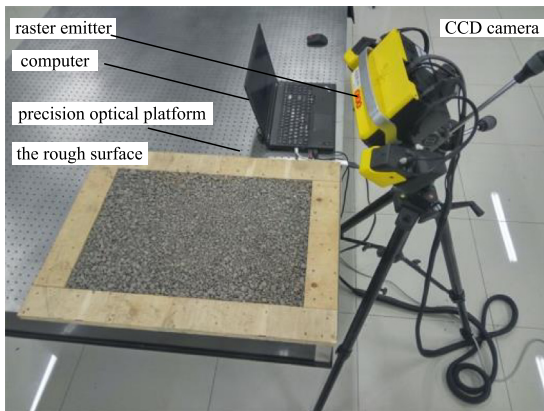
The process used to extract the surface features of the wall is illustrated in Fig. 2. To improve accuracy, multiple calibrations were carried out to provide optimal results. The calibration results demonstrate that the re-projection and alignment errors are 0.058818 mm and 0.019248 mm, respectively.

The rough wall used in the experiment (measuring 650 mm × 450 mm × 20 mm) was built using sand and stones and the scanning range used is 250 mm × 250 mm (Fig. 3). Due to the unevenness of the wall, all the data could not be obtained in one measurement. Instead, the experiment was carried out through a series of overlapping scans using marked points. The initial sample data obtained for the feature points were divided into several sets (see Table 1 which merely lists one set of partial data) and separately imported in the Geomagic Studio software package (Fig. 4a displays data on 13,386 feature points which covered 250 mm × 250 mm). In this way, a 3D point cloud model of the rough wall was constructed. After filtering the point clouds using Geomagic Studio, a 3D wall profile was generated (Fig. 4b).

Table 1

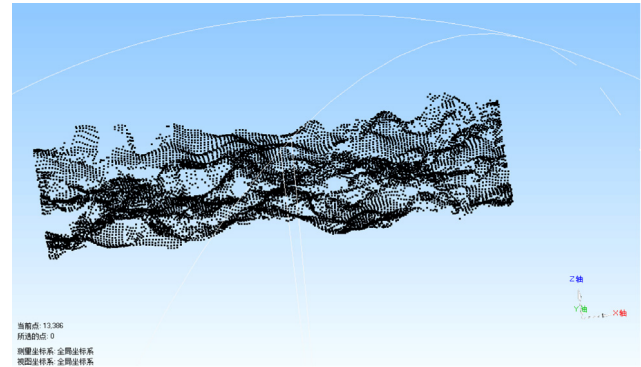
Partial set of data points for the wall's features (units: mm).

Exported selected points by TVScan 2012					
X-coordinate	Y-coordinate	Z-coordinate	X-coordinate	Y-coordinate	Z-coordinate
−34.8488	43.4914	77.4706	−32.3049	43.3026	77.4103
−34.6685	43.5279	77.3940	−32.0770	43.2601	77.4421
−34.4678	43.5308	77.3634	−31.8535	43.2249	77.4639
−34.2327	43.4778	77.4097	−30.8532	43.2415	77.3085
−33.9890	43.4103	77.4754	−29.1411	42.7420	77.8080
−33.7504	43.3510	77.5301	−28.9290	42.7244	77.8058
−33.5348	43.3293	77.5331	−28.7277	42.7247	77.7788
−33.3268	43.3199	77.5194	−28.5298	42.7308	77.7440
−33.1293	43.3280	77.4818	−28.3352	42.7423	77.7018
−32.9344	43.3401	77.4387	−28.1412	42.7550	77.6580
−32.7371	43.3483	77.4009	−27.9488	42.7701	77.6108

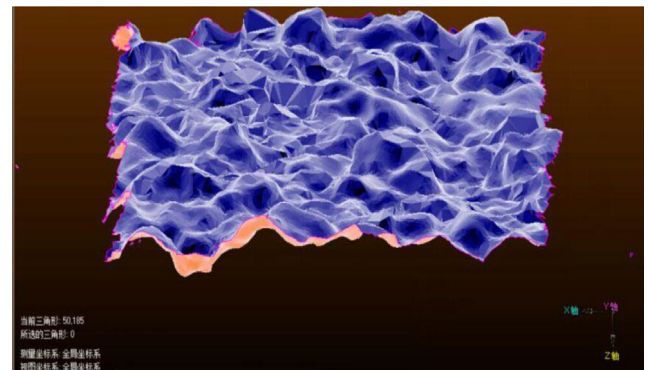
**Fig. 2.** The feature extraction procedure used on the rough wall surface.**Fig. 3.** The measurement experiment and rough wall.

2.3. Discriminant condition for the hooks to stably grip rough protuberances on the wall surface

Curves describing the protuberances on an arbitrary rough wall can be drawn according to the 3D surface profile data presented in Fig. 4. Depending on the characteristics of the curves, they can be partitioned according to their periods (the separation between two peaks is taken to be the period). Three typical curve types, labeled A, B, and C, can be found by summarizing the characteristics of each period (Fig. 5).



(a)



(b)

Fig. 4. The 3D features of the rough wall: (a) 3D point cloud model, (b) 3D profile.

A force analysis for A-type curves is demonstrated in Fig. 5d for when the hooks are attached to convex points. In the figure, α represents the normal angle (i.e. the angle between the direction of the contact normal between the hook and protuberance and the vertical plane), μ is the friction coefficient, and θ represents the grasping angle (i.e. the angle between the grasping force F and the negative y direction). The analysis reveals that the situation is stable if $F \sin \beta < N \mu$ and $F \cos \beta = N$. Thus, $\beta < \tan^{-1} \mu$, implying that the stability condition is,

$$\alpha < \theta + \arctan(\mu) \quad (1)$$

The condition given in Eq. (1) is the same as that for friction self-locking. For the A-type curve shown in Fig. 5a, AE is the period and it is clear that the upper hooks cannot grasp the wall in section CE while they may slide down along the wall in section AC. When Eq. (1) is satisfied, the claws will successfully grip the wall.

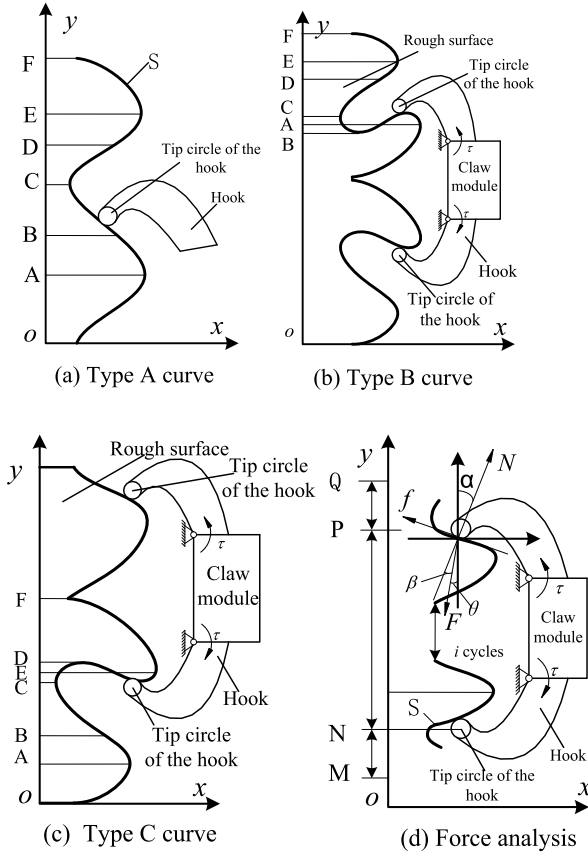


Fig. 5. Analysis of hooks gripping protuberances on the wall.

For B-type curves (Fig. 5b), there is a groove present (that is, there are multiple x values corresponding to a certain y value) so the claws can hook onto the groove directly. For C-type curves (Fig. 5c), the upper hooks cannot grasp the protuberance while the lower hooks can easily do so. The A-type curves correspond to when there are no grooves present. It can be seen that it is easy for the robot to grasp the wall surface when B- and C-type curves are present, so merely A-type curves need to be further analyzed.

3. Algorithm for the robot grasping a rough surface

In this section, we establish a point-contact model for the hook tip and 2D wall based on the preceding results. We also present an algorithm for extracting the points that can be gripped onto in the 2D wall. Then, using a triangular combination strategy for the spatial point cloud data, a discriminant algorithm to find positions that can be gripped onto is proposed based on the point cloud data from 3D walls.

3.1. Extraction algorithm for points that can be gripped onto for 2D walls

3.1.1. Contact model for miniature hooks and 2D wall profile

Here, we consider a 2D wall profile. Thus, the feature points derived using the measurement results from the 3D scanner are interpolated to produce a group of sample data, $M_{11}[x_{set}, y_{set}]$, in which x_{set} and y_{set} represent the sets of x - and y -coordinates of points in the wall profile. The profile curves constituted by these points approximately reflect the shape of the wall.

The cross-section of the hook and sample data $M_{11}[x_{set}, y_{set}]$ form a contact model for the wall profile (Fig. 6). The x -

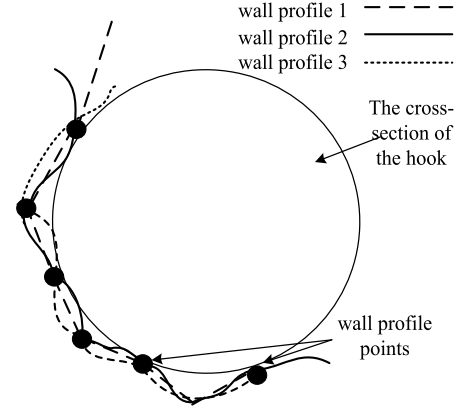


Fig. 6. Multi-point contact model of the hook and the wall.

coordinates of the data points in the matrix $M_{11}[x_{set}, y_{set}]$ denote the fluctuations in the wall while the y -coordinates are arranged incrementally along the positive direction of the y -axis. This is in accordance with wall surface information obtained using a 2D profiler and the results acquired through interpolation of the feature points.

For a wall profile described using data points (Fig. 7), three types of typical profile curves (ab , cd , and ef) can be obtained by summarizing the wall characteristics. The profile curve cd is the one mainly analyzed below. As the hook slips along the profile from c to d , it cannot reach all the points on the profile due to the unevenness of the wall surface (Fig. 6). To assess the gripping conditions of points on the wall profile, two contact points A and C are chosen as typical sample points. Choosing the center of the cross-section of the hook as the origin of coordinates, the local coordinate system shown in Fig. 7 is drawn. The coordinates of A and C are written as (x_A, y_A) and (x_C, y_C) , respectively. If A and C can be gripped, then they need to meet the following conditions:

(1) The distance from each point in the data set $M_{11}[x_{set}, y_{set}]$ to the origin of the coordinate system (the center of the cross-section of the hook) should not be shorter than the radius r , and $x_A^2 + y_A^2 = x_C^2 + y_C^2 = r^2$.

(2) According to Eq. (1), as the cross-section of the hook slips past the contact point, the vector pointing to the center of the cross-section of the hook shows an angle θ_b with the normal direction of the wall at the contact point. If the contact point meets the conditions that the y -coordinate is less than 0 and $\theta_b \geq \theta_{min}$, then the contact point can be gripped.

If the 2D wall profile is seen as being made up of a dense myriad of points, then the sliding of the hook on the wall is equivalent to sliding within a line segment connected by two adjacent points. If the two adjacent points are both contactable, then the line segment connecting the two points is a touchable region. The value of θ_b is related to the slope of the line segment, so it can be derived by calculating the slope. On this basis, we can judge whether the touchable region can be gripped or not.

3.1.2. Discriminant algorithm for miniature hooks gripping 2D walls

The judgment process for a set of irregularly-arranged points (Fig. 8) is as follows:

Step 1: Interpolation

To prevent overlapped spaces being considered between adjacent points, a datum length l is first defined (related to the size of the hook tips and scanning accuracy). Then, two adjacent points (x_i, y_i) and (x_{i+1}, y_{i+1}) ($i = 1, 2, \dots, n-1$) are selected from the sample data $M_{11}[x_{set}, y_{set}]$. If $(y_{i+1} - y_i)^2 + (x_{i+1} - x_i)^2 \leq l^2$ then the two adjacent points meet the spacing requirement;

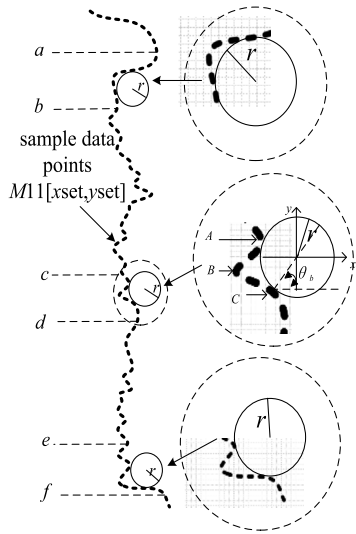


Fig. 7. Sketch map of the contact between the hook and the wall profile.

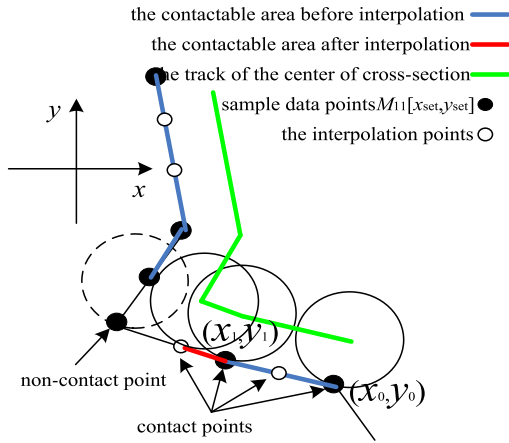


Fig. 8. The distribution of contact points.

otherwise, interpolation is conducted. For example, if the most simple form of interpolation (linear) is used, then a data point $((x_{i+1} + x_i)/2, (y_{i+1} + y_i)/2)$ is generated between the two points and used as the new point (x_{i+1}, y_{i+1}) . The above operation is then repeated for the new point (x_{i+1}, y_{i+1}) and (x_i, y_i) until the condition $(y_{i+1} - y_i)^2 + (x_{i+1} - x_i)^2 \leq l^2$ is satisfied. Then, the next pair of points undergoes this operation until the whole data sample is interpolated.

Step 2: Select contactable points

Two adjacent points are selected (in order) from the sample data (starting with the first point and moving systematically through them, as before) and used to form a line segment. Then, according to the coordinates of the two points and the radius r of the cross-section of the hook, the coordinates of the center of the circle outside the wall corresponding to the end points of the line segment are calculated. Taking point (x_i, y_i) as an example, suppose that the coordinates of the corresponding circle center are (x_{0i}, y_{0i}) . Then, this point obeys the following equation:

$$(x_{0i} - x_i)^2 + (y_{0i} - y_i)^2 = r^2 \quad (2)$$

Meanwhile, the slope of the line segment is $k_i = (y_{i+1} - y_i)/(x_{i+1} - x_i)$. Let $k'_i = -1/k_i$, then k'_i refers to the slope of the perpendicular line drawn from the circle center to the line segment. The perpendicular line, however, passes through both

(x_i, y_i) and (x_{0i}, y_{0i}) and so the coordinate of the circle center also obeys the following equation:

$$y_{0i} - y_i = -\frac{1}{k'_i}(x_{0i} - x_i) \quad (3)$$

By simultaneously solving Eqs. (2) and (3), the coordinates of two circle centers, (x_{0i1}, y_{0i1}) and (x_{0i2}, y_{0i2}) , can be obtained. In this section, the solution with the larger x value is always taken as the coordinates of the center of the circle outside the wall. Based on the circle center derived, the distances of the points in the sample data $M_{11}[x_{set}, y_{set}]$ from the circle center can be calculated. If the distance from a point to the circle center is shorter than the radius r of the circle, the contact condition is not satisfied, and so the line segment is rejected. Then, the next pair of points is chosen and Step 2 is repeated. If the two ends both meet the contact condition, then the two points are contactable and the line segment between the two points is a contactable region. Then, the procedure turns to Step 3.

Step 3: Check for graspability

A perpendicular line is drawn from the circle center to the contact line and the angle it makes with the vertical direction is calculated (Fig. 8). If the contact angle of the line segment between (x_0, y_0) and (x_1, y_1) is θ , then $\theta_b = \pi/2 - \theta$. If $\theta_b \geq \theta_{min}$, then the line segment is a region that can be grasped and the end points of the line segment can be grasped.

By repeating Steps 2 and 3 for each group of adjacent points in the sample data $M_{11}[x_{set}, y_{set}]$, all the points and regions that can be grasped are finally obtained. The algorithm required to implement the procedure is illustrated in Fig. 9.

3.2. Discriminant algorithm for the graspable positions on 3D walls

Given point cloud data describing a 3D wall profile, the triangle formed by three adjacent points is used in place of the wall profile of the region. The places that can be contacted with the hook can therefore be judged by partitioning the point cloud data into a myriad of triangular regions. Then, all the contactable regions identified can be checked to see whether they can be grasped according to the discriminant conditions for gripping.

3.2.1. Judging if a region is graspable or not

Each point in the data has coordinate information related to a set of x -, y -, and z -axes and the points collectively form a surface that is spatially curved. In this research, a triangular-combination strategy is proposed to deal with the point cloud.

The contact between the hook and the wall surface can be treated as being equivalent to that between the hook and triangles formed by the point clouds of the wall (Fig. 10). In Fig. 10b, the triangle $\triangle ABC$ formed by the points A, B, and C is regarded as representing the appearance of the surface in this region. If there is a point D above $\triangle ABC$, then the region $\triangle ABC$ can be partitioned into a protuberance in the form of a triangular pyramid. As the hook slides in the region, it makes contact with faces a , b , and c . The point cloud data are subjected to triangular combination. According to the radius of the tip of the hook, all the contactable triangular combinations are found via a process of traversal based on the coordinates of the points. On this basis, the contact angles between the hook and each triangle are computed. Then, in accordance with Eq. (1), it is determined whether the triangle can be grasped or not.

In 3D space, the tip of the hook is a hemisphere and the 3D wall profile is equivalent to the spatial point cloud data. The contactable condition in this case can be expressed in the form: if three points can be contacted with the tip of the hook, then the triangle formed by the three points is a contactable triangle.

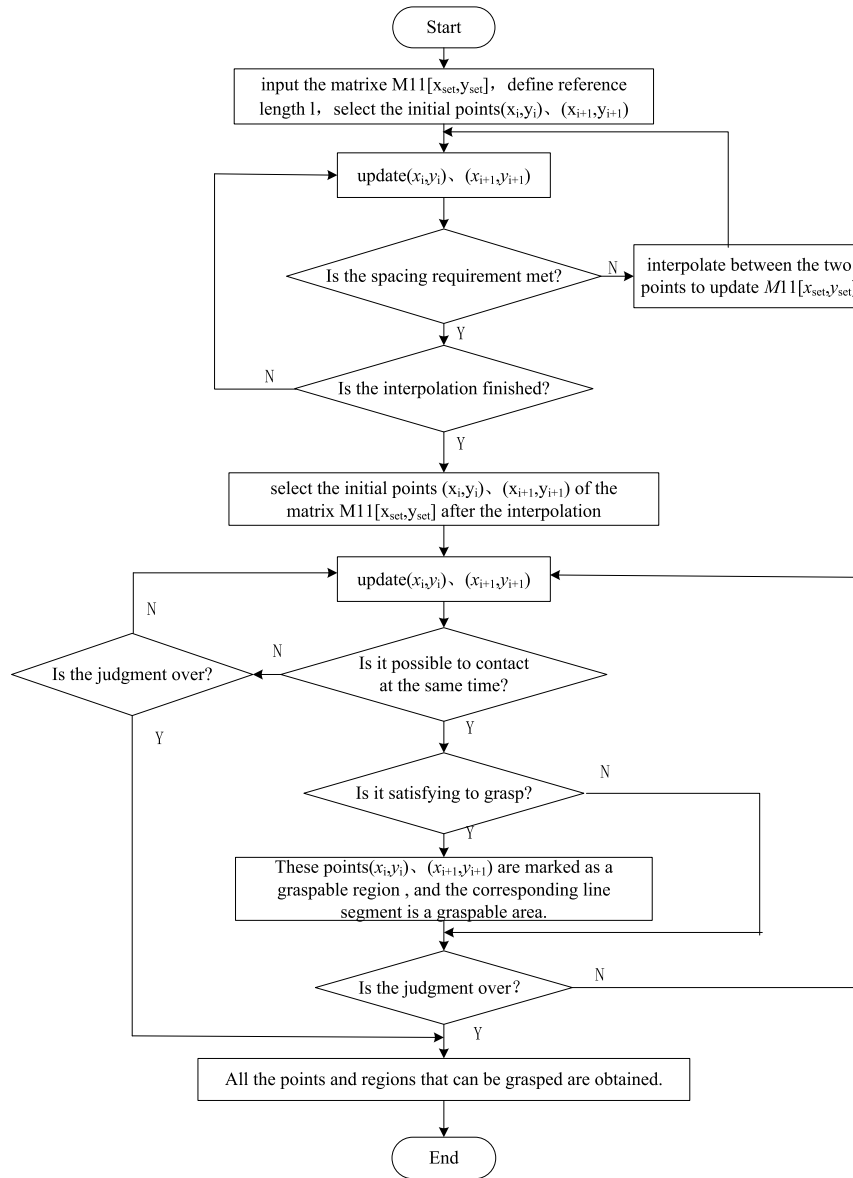


Fig. 9. The algorithm used to carry out the grasping point selection procedure.

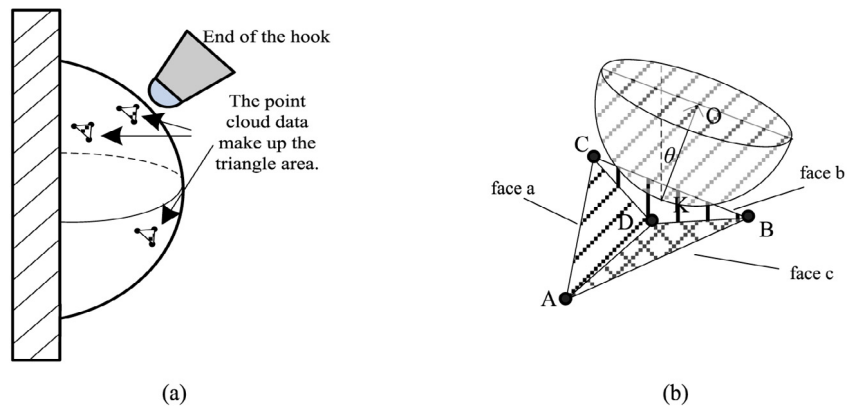


Fig. 10. Contact models for the hook-wall contact: (a) contact model of the spherical asperity composed of point clouds, (b) contact model of the hook and a pyramid convex to the wall.

A spherical model is used to analyze the contact between the tip of the hook and the spatial point cloud (Fig. 11). Seven

points, A–G, are randomly selected from the surface. It is further assumed that any arbitrary set of three of these points are not

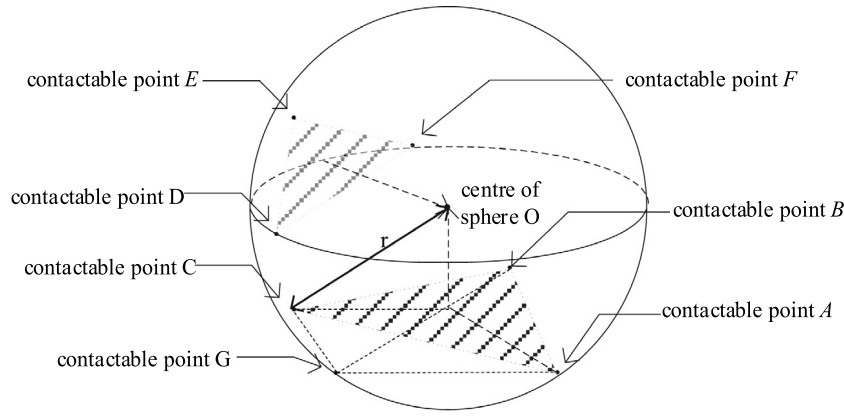


Fig. 11. Contact model of the spatial points and a sphere.

collinear, so that the seven points form 35 unique triangles. The contact between the multitude of spatial points and the sphere can therefore be decomposed into that with several triangles. Taking the triangle $\triangle ABC$ formed by the contact points A, B, and C as an example, the constraints for contact being made between the three vertices of the triangle and a sphere of given radius are as follows:

Constraint 1. The length of each arbitrary side (AB , AC , or BC) of triangle $\triangle ABC$ should not be longer than the diameter of the sphere, $2r$, that is,

$$\begin{cases} |\vec{AC}| \leq 2r \\ |\vec{AB}| \leq 2r \\ |\vec{BC}| \leq 2r \end{cases} \quad (4)$$

Constraint 2. The area of $\triangle ABC$ needs to be smaller than or equal to the largest area of an inscribed triangle of the sphere. The inscribed triangle that passes through the center of the sphere has the largest area. Suppose that the central angles corresponding to each side of an inscribed triangle are α_0 , β_0 , and γ_0 ($\alpha_0 > 0$, $\beta_0 > 0$, $\gamma_0 > 0$, and $\alpha_0 + \beta_0 + \gamma_0 = 2\pi$). Then, the area of the triangle is $S = r^2(\sin \alpha_0 + \sin \beta_0 + \sin \gamma_0)/2$ and the extremum is obtained when $\alpha_0 = \beta_0 = \gamma_0 = 2\pi/3$, in which case $S = 3r^2(2\pi/3)/2 = 3\sqrt{3}r^2/4$. According to Heron's formula, the area of a triangle is given by $S = \sqrt{p(p-AB)(p-AC)(p-BC)}$ where $p = (AB + AC + BC)/2$. Therefore, the three sides of $\triangle ABC$ need to obey the relationship

$$0 < \sqrt{p(p-AB)(p-AC)(p-BC)} \leq 3\sqrt{3}r^2/4 \quad (5)$$

Constraint 3. Points inside deep grooves or small cracks are probably not contactable. The contact points A, B, and C are all located at a distance r away from the center of the sphere and the sphere does not contain any other spatial points inside. That is, an arbitrary point in the space, $P(x_i, y_i, z_i)$, must lie a distance away from the center of the sphere of at least r . Overall, we have

$$\begin{cases} |\vec{AO}| = r \\ |\vec{BO}| = r \\ |\vec{CO}| = r \\ |\vec{PO}| \geq r \end{cases} \quad (6)$$

Three spatial points simultaneously meeting the above three constraints constitute a contactable triangle.

In the above analysis, the precondition of [Constraint 3](#) is that the coordinates of the center of the sphere are known. However in practice, the coordinates of the center are unknown. A method of finding the coordinates of the center of the sphere based on the coordinates of three spatial points and the radius r is described as follows.

[Fig. 11](#) shows the location of the center of the sphere corresponding to the spatial triangle. In the algorithm, the *solve* function in MATLAB is used to convert the problem to finding the symbolic analytical solution of a set of algebraic equations. The procedure in MATLAB is written as:

$$\begin{aligned} &\text{syms } x, y, z; \\ &[x, y, z] = \text{solve}(r^2 - (x - x_A)^2 - (y - y_A)^2 - (z - z_A)^2, \\ &\quad r^2 - (x - x_B)^2 - (y - y_B)^2 - (z - z_B)^2, \\ &\quad r^2 - (x - x_C)^2 - (y - y_C)^2 - (z - z_C)^2); \end{aligned}$$

When merely [Constraints 1](#) and [2](#) are met, the solutions found for the coordinates of the center of the sphere will probably not be real. For this reason, imaginary solutions need to be eliminated during the computation. In this research, the coordinate information relating to the z -axis of the point clouds reflects the fluctuations in the wall profile. As the hook tip contacts the point clouds in a downwards manner, the solution with the largest z value is always taken if there are multiple solutions.

After solving for the coordinates of the center of the sphere, the angle between the normal vector of the contact triangle (pointing towards the center of the sphere) and the reverse direction of the movement of the hook is the contact angle. The normal vector of $\triangle ABC$ is written as

$$\vec{n} = \frac{\vec{AB} \times \vec{AC}}{|\vec{AB} \times \vec{AC}|} \quad (7)$$

To guarantee that \vec{n} always points to the center of the sphere, an arbitrary point on $\triangle ABC$ is selected. Taking the vertex A as an example, the vector \vec{AO} connecting A to the center of the sphere O is constructed. If the angle between \vec{AO} and \vec{n} is less than 90° , then we set $\vec{n}_{ABC} = \vec{n}$; otherwise, we set $\vec{n}_{ABC} = -\vec{n}$. The angle between the resulting vector and the reverse direction of the movement of the hook (supposing that the hook moves in the negative direction of the y -axis) represents the contact angle between the hook tip and the triangle. Then, whether or not the triangle meets the gripping constraints can be judged based on [Eq. \(1\)](#).

3.2.2. Procedural steps and algorithm

First, we outline the steps involved in the discrimination process, and then present the corresponding algorithm.

Step 1: The hook size r and minimum graspable angle θ_{\min} are defined. To prevent an overlapped space between adjacent points, the final point cloud sample $M_{21}[x_{\text{set}}, y_{\text{set}}, z_{\text{set}}]$ is obtained by conducting interpolation on the initial set of point clouds based on the hook size r .

Step 2: All three-point combinations probably forming contactable triangles are acquired by traversal through the point cloud sample $M_{21}[x_{\text{set}}, y_{\text{set}}, z_{\text{set}}]$ and using Eqs. (4) and (5) – put them into $M_{22}[x_{\text{combine}}, y_{\text{combine}}, z_{\text{combine}}]$.

Step 3: Then, each combination in $M_{22}[x_{\text{combine}}, y_{\text{combine}}, z_{\text{combine}}]$ is tested to see if it satisfies **Constraint 3**:

(1) The three points in the current combination (and radius r of the hook tip) are used to find the corresponding center of the sphere. If the result is real, move on to (2); otherwise, go back to Step 3 to test the next combination.

(2) Using the center of the sphere derived (taking the one with larger z -coordinate, if there are two solutions), the distances of the points in $M_{21}[x_{\text{set}}, y_{\text{set}}, z_{\text{set}}]$ to the center of the sphere are calculated through traversal. If there is no point whose distance to the center of the sphere is shorter than r , the current three points and the corresponding center of the sphere are placed in matrix M_{23} and then the next combination is judged by returning to Step 3. This is continued until all combinations in M_{22} have been tested.

Step 4: The vector normal to the contact triangle is derived according to Eq. (7) and checked to make sure it points to the center of the sphere – then the contact angle θ between the hook and the contact triangle is calculated. Using the condition $\pi/2 - \theta > \theta_{\min}$, it is found that the angle satisfies the grasping constraint. If it does, the group of points are put into matrix M_{24} .

Step 5: The next group of points in M_{23} is taken and judged as in Step 4. Judgment continues until all the combinations have been judged and all graspable positions acquired.

3.2.3. Simulations

To check the performance of the algorithm with respect to the numbers and positions of graspable points discovered, simulations were performed using the MATLAB software package. Some of the initial point clouds in Section 2.3 are selected as experimental data and interpolation conducted using a cubic method. Theoretically, the smaller the space between points after interpolation the better. However, a spacing that is too small will lead to an excessive number of calculations being undertaken. In this work, the wall surface is profiled according to the hook size ($r \geq 10 \mu\text{m}$) of the claw tip and so an interpolation spacing of $4 \mu\text{m}$ is adopted (Figs. 13–15). As the wall profile appears as point clouds, the change in the z -coordinates of the data points reflects the fluctuations in the wall surface. We also assume that the hook always moves along the negative direction of the y -axis.

As the algorithm is based on certain geometric relationships, the effect of hook size r and θ_{\min} on the number of graspable points is only discussed. The triangles formed by adjacent graspable points will probably overlap, resulting in calculated areas that are inaccurate. Thus, the number of graspable points is used as the measurement criterion when analyzing the simulations.

The point clouds making up the wall surface are shown in Fig. 12 (1176 points are shown) and black asterisks are used to

represent the graspable points. The heights of the wall surface are represented using different colors. It can be seen from the simulations that the lower and upper regions of convex peaks cannot be grasped when a hook moves in the negative y -direction. Near the bottoms of the pits in the wall surface, there are some regions that do satisfy the grasping angle condition but cannot contain the hook. Therefore, these regions are regarded as not satisfying the contact conditions.

Comparing Fig. 12a and b, it can be seen that the number of graspable points is significantly reduced when the value of r is increased. By comparing the M_{24} matrices in these two simulations, the numbers of graspable points are found to be 104 ($r = 10 \mu\text{m}$ and $\theta_{\min} = 40^\circ$) and 46 ($r = 20 \mu\text{m}$ and $\theta_{\min} = 40^\circ$). The reason for the difference in graspable point is that, for a given wall surface, the region between two convex peaks and pits will be less likely to accommodate the hook when the latter grows in size. Thus, the number of contactable regions and graspable positions is reduced accordingly. Comparing Fig. 12a and c, the number of graspable points is also significantly decreased if θ_{\min} is made larger (the M_{24} matrices indicate that there are 104 graspable points in Fig. 12a, where $\theta_{\min} = 40^\circ$, and 73 in Fig. 12c, where $\theta_{\min} = 50^\circ$).

The three simulations in Fig. 12 also show that there are multiple ungraspable points near the boundary region corresponding to $y = 120 \mu\text{m}$. This is because we have assumed that the hook moves in the negative y -direction during the simulations and $y = 120 \mu\text{m}$ corresponds to the initial position. Therefore, **Constraint 3** partially fails.

Further simulations were made using diverse wall surfaces with different asperity. The simulation results using the same parameters as before are shown in Figs. 13 and 14 (Fig. 13 consists of 1436 point clouds and Fig. 14 1176). Comparing the M_{24} matrices, as before, it is found that the numbers of graspable points in Fig. 13 are 272, 114, and 191 for cases (a)–(c) (corresponding to $r = 10 \mu\text{m}$, $\theta_{\min} = 40^\circ$; $r = 20 \mu\text{m}$, $\theta_{\min} = 40^\circ$; and $r = 10 \mu\text{m}$, $\theta_{\min} = 50^\circ$), respectively. The corresponding numbers in Fig. 14 are 67, 46, and 56, respectively.

In light of the simulation results, the following conclusions can be drawn: (i) the smaller the radius r of the hook, the greater the number of graspable points; and (ii) the smaller the minimum graspable angle θ_{\min} , the greater the number of graspable points. The smaller the radius of the hook, the more points can be grasped stably, therefore, we should minimize the size of the sharp hook as far as the strength of the material allows. As the size of the sharp hook is reduced, the robot will also change in terms of load, therefore, the size of the robot should match the size of the sharp hook. Thus, we must design the wall-climbing robot so that it has a reasonable body size, a hook tip that is as small as feasible, and a friction coefficient (between the hook and wall surface materials) that is as large as possible.

4. Experiments

A wall-climbing robot is likely to be affected by wall vibration and wind loads during high-altitude assignments and other operations in the field. Therefore, it is prone to turning over and dropping from the wall surface. Hence, in this section, a vibration platform is used to conduct grasping experiments on the claws.

4.1. Claw mechanism and experimental platform

4.1.1. Grasping claw module

Prototype claws were manufactured according to the claw model given in Section 2.1 (Fig. 15). The hooks were manufactured from #45 steel and the hook tips were subjected to nitriding treatment to enhance their wear resistance. Elastic steel sheets

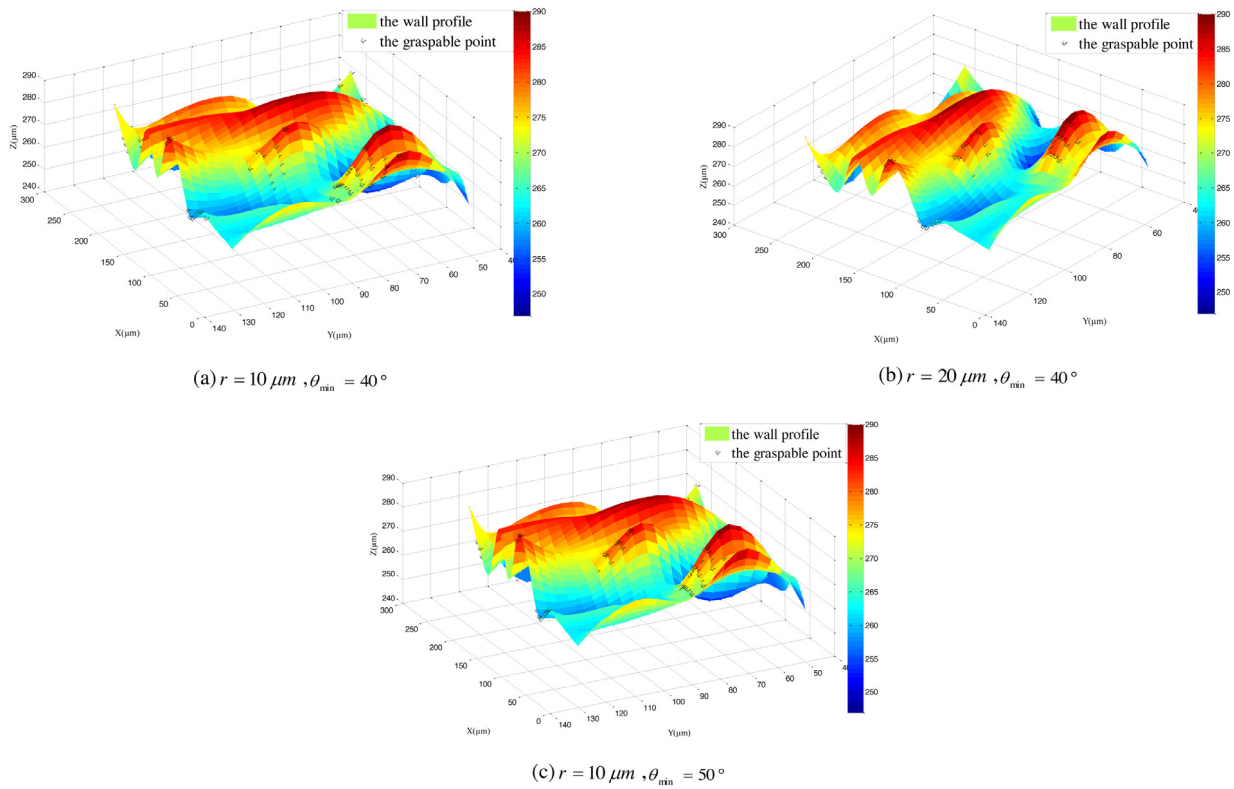


Fig. 12. Simulation results obtained using the algorithm (1176 points).

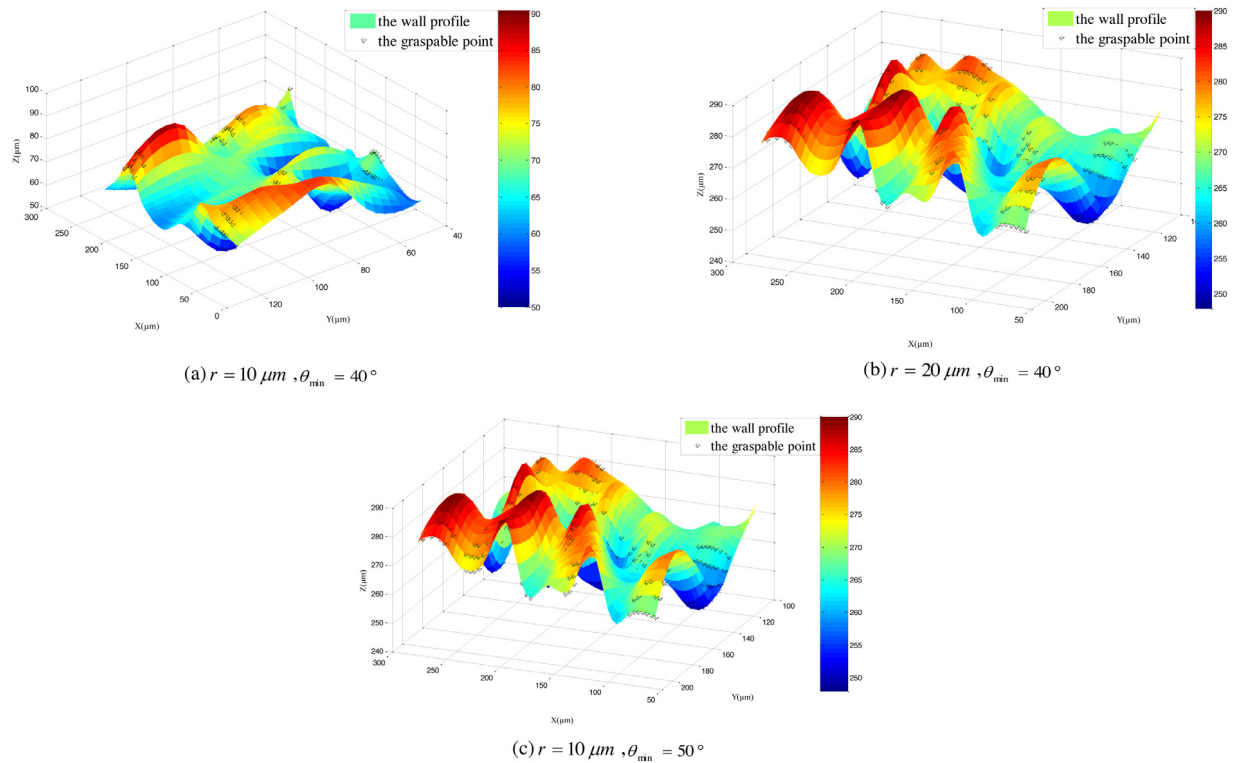


Fig. 13. Further simulation results obtained using the algorithm (1436 points).

made of 65Mn steel were subjected to surface finishing and their holes were smoothed to avoid concentration of stress. The claw bodies were prepared from aluminum alloy. According to the results of a modal analysis, the natural frequencies of the claws

lie in the range 394–728 Hz (thus, these frequencies must be avoided). The experiments used a vehicle-mounted pump as a power source. This was connected to an actuating cylinder via a pressure control valve. In this way, the pressure in the cylinder

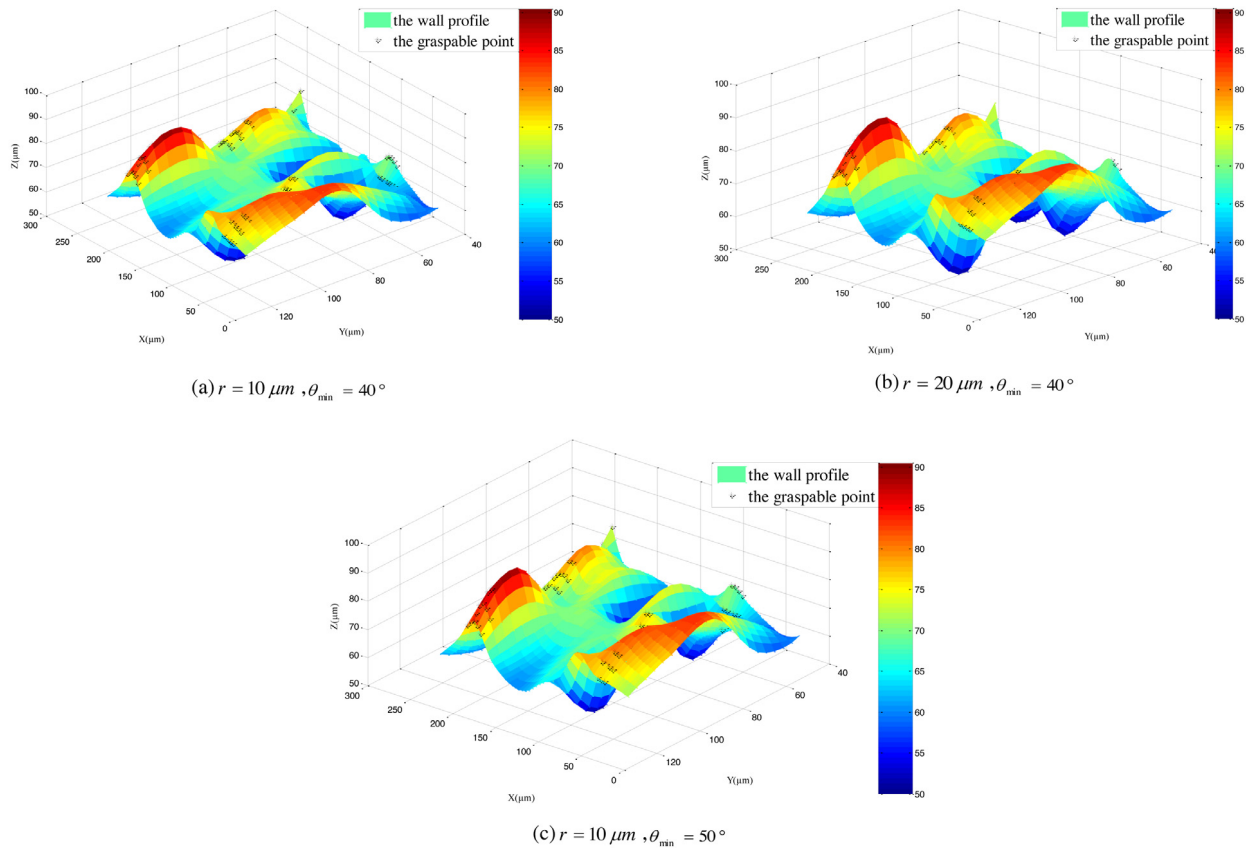


Fig. 14. Further simulation results obtained using the algorithm (1176 points).

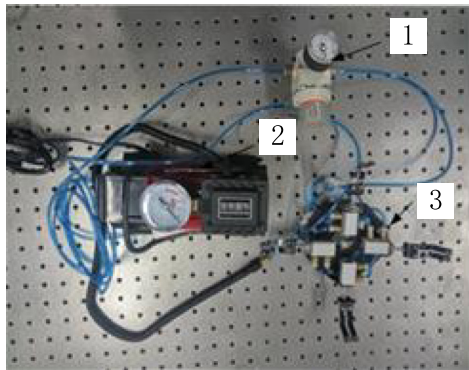


Fig. 15. The grasping system of claws (key: 1 — Pressure control valve; 2 — Vehicle-mounted pump; 3 — Claws).

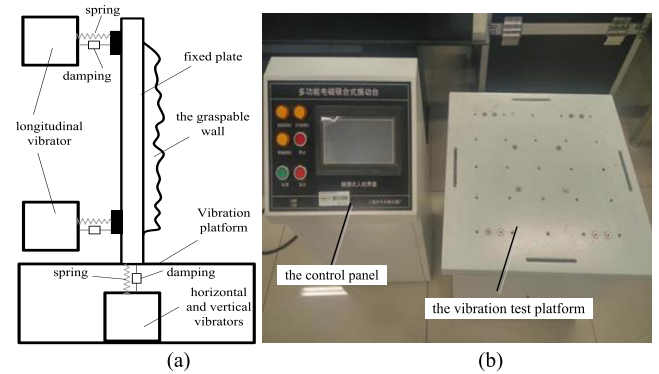


Fig. 16. Details of the experimental platform: (a) Schematic diagram; (b) Electromagnetic vibrator.

could be adjusted using the pressure control valve to allow the driving force to be controlled. The total mass of the claws is 431 g and the maximum stroke of the cylinder was 1.75 cm. The driving force applied by the cylinder to the spiny feet is 12.7 N when the vehicle-mounted pump is operated normally.

4.1.2. Test platform (vibrating wall surface)

Electromagnetic suction vibrators (parameters shown in Table 2) were used to establish a vibrating test platform (Fig. 16a). The platform was used to simulate a vibrating wall by adjusting the amplitudes and frequencies of the vibrators.

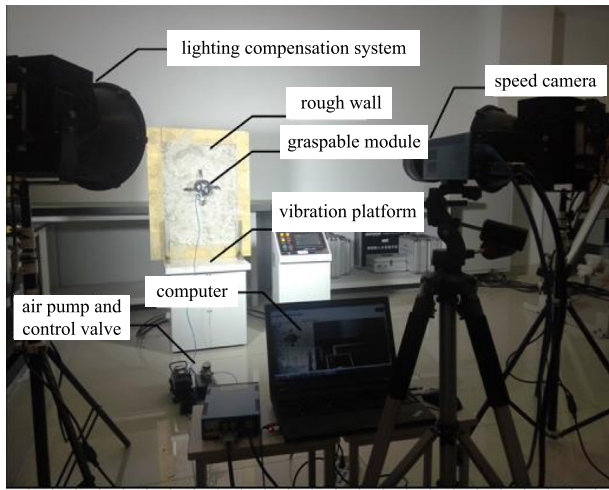
The grasping performance of the claws was verified by preparing and installing various rough walls with various kinds of pits and protuberances. Surface roughness is the basic morphology of solid surface. At present, there are 34 terms and definitions

about the surface, contour and reference, 11 surface roughness parameters related to the height characteristics of micro-convex bodies, 11 transverse spacing characteristic parameters and 7 shape characteristic parameters [39]. The rough wall used in the experiment is the wiper stone wall made in the laboratory. The roughness of contour line is about $R_a = 93.0 \mu\text{m}$, and the roughness of Root-Mean-Square of contour is about $R_q = 130.0 \mu\text{m}$. Its roughness is similar to that of concrete walls in real life. Its roughness is similar to that of actual concrete walls. The claw can be attached to the walls where the roughness of contour lines is greater than $R_a = 93.0 \mu\text{m}$ and the RMS roughness exceeds $R_q = 130.0 \mu\text{m}$. Experiments were then conducted on the claws to investigate their resistance to vibration and turnover.

Table 2

Parameters of the electromagnetic vibrators.

Maximum load	100 kg	Power	0.75 kW~2.2 kW
Maximum acceleration	<20 g	The vibration direction	X + Y + Z
Maximum amplitude	0~5 mm	Precision	0.01 Hz
Frequency range	1~600 Hz	Frequency sweep	1~600 Hz

**Fig. 17.** Photograph showing a grasping test on the vibrating wall surface in progress.

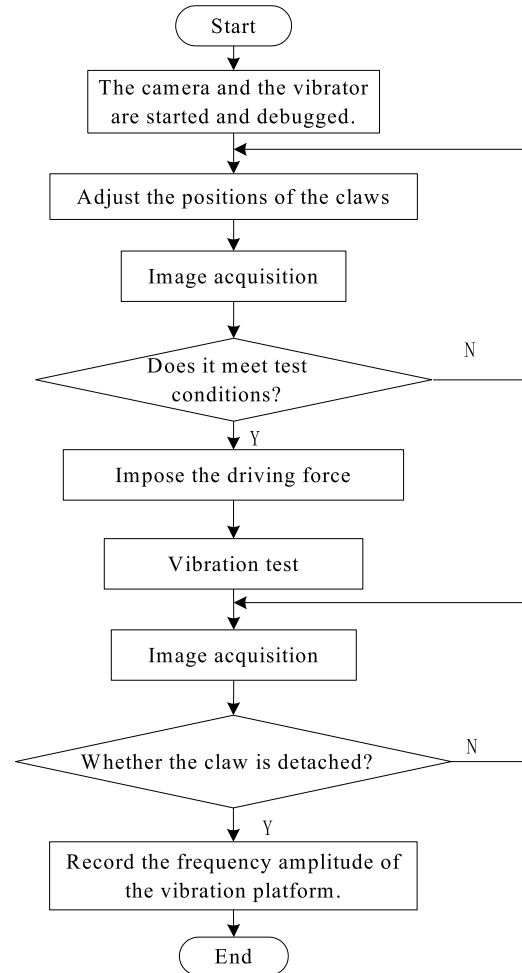
The experiments were fulfilled with the assistance of a high-speed camera system which allows the test object to be monitored without disturbing it (Fig. 17). Measurements can be completed without touching the claws and information relating to the displacement and acceleration of marked points can be acquired after completing the experiment. The image sequences were processed using appropriate software to extract the important physical information from all the frames in the sequences.

The image acquisition system consists of a high-speed camera system (PCO.1200 s/hs, Germany) and an image analysis system. To allow the vibrations of the wall to be followed, the camera was set to use a resolution of 1280×1024 and capture rate of 500 frame/s.

To begin with, the vibration resistance of the claws, with and without a driving force (hanging mode) were separately evaluated. This was accomplished using a frequency-scanning function of the vibrator system. By setting the low and high frequencies used, as well as the low and high vibration intensities of the vibrator, the frequency and amplitude of the wall, as well as the dead time at various frequencies and amplitudes, could be controlled.

A flow chart for the frequency-scanning experiment is shown in Fig. 18. The main steps involved are:

- (1) First, the high-speed camera system and the vibrator are started and debugged.
- (2) Then, the regions on the rough wall where the claws can stably hook onto are explored and marked. The positions of the claws are adjusted so that the claws can stably grasp the wall under the influence of the driving forces.
- (3) Main test is started. The high-speed camera is used to record various parameters (output frequency and amplitude of the vibrators) and separately record the output frequency and intensity of the test platform when the claws become detached from the wall, before and after imposing the driving forces.

**Fig. 18.** Flow chart for the frequency-scanning experiment.

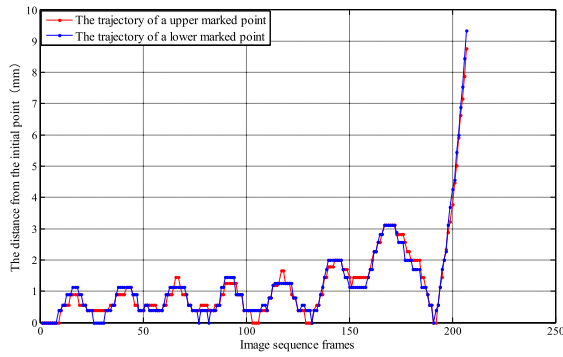
4.2. Vibration experiments and analysis of results

4.2.1. Vibration experiments

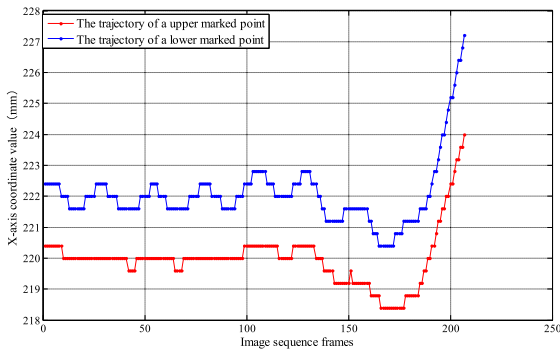
The grasping ability of the claws was determined with and without a grasping force applied. The maximum endurable frequency and intensity of the claws with a grasping force measured via a longitudinal frequency-scanning experiment are 12.3 Hz and 76.2% (the amplitude of the vibrator was 1.5875 mm). When the claws do not bear a grasping force the corresponding figures are found to be 12.3 Hz and 20.1% (the amplitude of the vibrator was 0.41875 mm).

This result clearly indicates that taking advantage of the grasping mode can significantly improve the vibration resistance of the claws. In order to further investigate these results, further grasping experiments on the claws under a driving force were carried out in two phases: (i) a stable grasping phase after imposing a driving force, and (ii) a detaching phase without a driving force. The transition between these two phases was realized by shutting off the control valve.

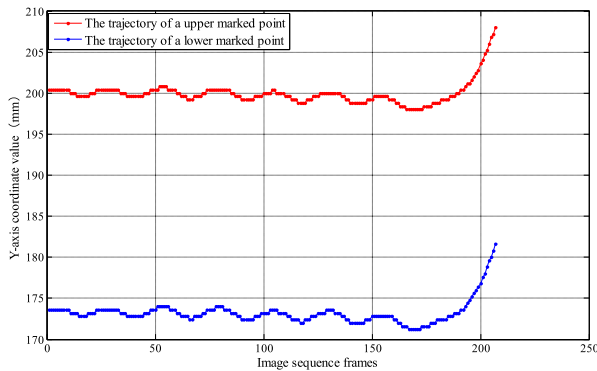
During these experiments, the output frequency and intensity of the vibrator were set to 12 Hz and 60%, respectively. To



(a) Displacement of the marked points from the initial positions



(b) Change in x-coordinate of the marked points



(c) Change in y-coordinate of the marked points

Fig. 19. Image sequence analysis for the first 208 frames.

intuitively and accurately describe the detachment process of the claws, images were recorded using the high-speed camera before and after turning off the control valve. These were imported into the image analysis software (Image Pro). The pixel information was transformed into actual length units by calibrating the images. The spatial calibration was conducted using the set of marked points (6 mm in size). The marked points were traced after the calibration process.

4.2.2. Results analysis

The upper and lower two marked points of the claws can thus be traced to yield the movement tracks shown in Fig. 19. In Fig. 19, the horizontal axes all correspond to the frame number in the image sequence. The vertical axes relate to the positions of the marked points (e.g. in (b) and (c) the x- and y-coordinates of the marked points are plotted, respectively).

4.2.3. Comparison of vibration resistance before and after imposing the driving force

It was found from the vertical frequency-scanning experiments that the output frequency and intensity of the vibrator corresponding to the maximum endurable disturbance, with the driving force imposed, are 12.5 Hz and 108.2% (amplitude: 2.2547 mm), respectively. Without the driving force these data become 12.5 Hz and 33.1% (amplitude: 0.6895 mm), respectively.

The output frequency and intensity of the vibrator were then set to 12 Hz and 80% (amplitude: 1.6667 mm). These were then tracked using the image processing software. Once again, a comparison was made between the vibration performances of the claws before and after imposing the driving force.

4.2.3.1. With the driving force. We set five markers on the gripper capture module and tracked the trajectory of the five markers through image processing software. Since the five marker points are in different positions on the same fetching module, the five points have a mutually synchronous relationship. We find that when the driving force is applied, the hook claw grasping module can still attach the hook to the wall surface in a stable manner with the vertical vibration of the wall surface. Among them, the amplitude of the marker located in the upper claw, and the amplitude of the other markers, showed a slight change. It was found that the vibration of the wall caused the lower claw to slide down the wall over a short distance. The gripper attachment positions, as distributed on both sides of the gripper module, have also been adjusted accordingly.

4.2.3.2. Without the driving force. After the claws are allowed to grasp the wall surface in the normal manner, the operator shuts off the pressure control valve and stops the vibration of the experimental platform. Then, after the air pressure inside the actuating cylinder has been balanced with external pressure, the experimental platform is restarted and vibration tests are made in the absence of the driving force. The results are illustrated in Fig. 20. The horizontal axis again represents the frame number of image sequence and the vertical axis is the displacement from the initial position.

It can be speculated through this analysis that the secondary claw on the right side (cyan curve in Fig. 20) first is detached from the wall under the effect of the external disturbance, at which time the claws appear to roll over. Afterwards, the marked points on the secondary claws on the left side, lower secondary claw, and main body all become greatly displaced from their initial positions. This indicates that these parts are detached from the wall surface successively and that eventually the upper secondary claw also loses attachment to the wall (red curve in Fig. 20).

The comparison experiments above show that the designed claws arranged in a cross exhibit a better vibration and turnover resistance in grasping mode than in traditional hanging mode. Comparing horizontal and vertical directions, there is a more significant effect on the grasping performance of the claws when the direction of the external incentive is vertical with respect to the wall surface.

5. Conclusions

(1) In this work, we put forward a structure in which claws are arranged in a cross and deduce the mechanical conditions for locking to occur between hooks on the claws and protuberances on the walls from the perspective of friction self-locking. We also propose that walls should be scanned using a 3D scanner and a method of extracting the roughness characteristics of the wall is provided. Our simulation results imply that 2D and 3D morphologies of rough walls can be reproduced using profile curves and point clouds.



Fig. 20. The displacements of the various marked points on the claws. (For interpretation of the references to colour in this figure legend, the reader is referred to the web version of this article.)

(2) A discriminant algorithm to locate the graspable positions of a 2D wall is proposed. On this basis, a contact model for spatial points is analyzed and a triangulation method is put forward for use with 3D walls. The effectiveness of the discriminant algorithm with respect to graspable positions on 3D walls was verified via simulations and the effect of the radius r of the hooks and minimum graspable angle θ_{\min} on the number of graspable points found on walls was deduced. The following conclusions can be drawn in light of the simulation results: for rough walls described using point clouds, the smaller the radius r of the hook, the greater the corresponding number of graspable points found; similarly, the smaller the minimum graspable angle θ_{\min} , the more abundant the number of graspable points. This means that we must design the wall-climbing robot so that its body size is reasonable, make the size of the hook tips as small as possible, and increase the friction coefficient between the hooks and wall surfaces. The algorithm can judge and locate the graspable points on rough walls and is a practical algorithm that can be used to help wall-climbing robots grasp walls.

(3) A vibrating test platform was established to carry out grasping experiments on the claws. A high-speed camera was used to visually trace a number of marked points on the claws and monitor its grasping performance. The maximum endurable disturbances after imposing a driving force was 12.5 Hz and 108.2% (amplitude: 2.2547 mm). The corresponding figures without the driving force are 12.5 Hz and 33.1% (amplitude: 0.6895 mm). The feasibility of the discriminant algorithm for the graspable positions on 3D walls and the stability of the gripper are verified.

In the future, we plan to investigate methods for identifying the graspable regions of a wall more thoroughly. As part of this investigation, it is intended that a visual detection algorithm will be employed to more purposefully look for graspable points. In addition, if the algorithm is applied to a climbing robot, it is necessary to carry a micro-scanner on the robot, scan the wall with a micro-scanner, determine the grabbing point, and adjust the posture to achieve the grab. This is one of our next priorities.

Declaration of competing interest

The authors declare that they have no known competing financial interests or personal relationships that could have appeared to influence the work reported in this paper.

Acknowledgments

This project is supported by the National Natural Science Foundation of China (51775284), Primary Research & Development Plan of Jiangsu Province (BE2018734), Joint Research Fund for Overseas Chinese, Hong Kong and Macao Young Scholars (61728302), and Six talent peaks project in Jiangsu Province (JY-081).

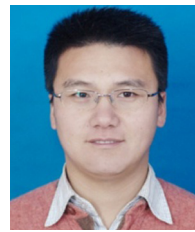
Appendix A. Supplementary data

Supplementary material related to this article can be found online at <https://doi.org/10.1016/j.robot.2020.103501>.

References

- [1] X. Gao, D. Xu, Y. Wang, H. Pan, W. Shen, Multifunctional robot to maintain boiler water-cooling tubes, *Robotica* 27 (06) (2009) 941–948.
- [2] M. Tavakoli, C. Viegas, L. Marques, J. Pires, A. de Almeida, OmniClimbers: Omni-directional magnetic wheeled climbing robots for inspection of ferromagnetic structures, *Robot. Auton. Syst.* 61 (9) (2013) 997–1007.
- [3] J. Li, X. Gao, N. Fan, K. Li, Z. Jiang, Adsorption performance of sliding wall-climbing robot, *Chin. J. Mech. Eng.* 23 (06) (2010) 733–741.
- [4] B. Hu, L. Wang, Y. Zhao, Z. Fu, A miniature wall climbing robot with biomechanical suction cups, *Ind. Robot: Int. J.* 36 (6) (2009) 551–561.
- [5] W. Wang, K. Wang, G. Zong, D. Li, Principle and experiment of vibrating suction method for wall-climbing robot, *Vacuum* 85 (1) (2010) 107–112.
- [6] I. Koo, T. Trong, Y. Lee, H. Moon, J. Koo, S. Park, H. Choi, Development of wall climbing robot system by using impeller type adhesion mechanism, *J. Intell. Robot. Syst.* 72 (1) (2013) 57–72.
- [7] R. Liu, R. Chen, H. Shen, R. Zhang, Wall climbing robot using electrostatic adhesion force generated by flexible interdigital electrodes, *Int. J. Adv. Robot. Syst.* 10 (36) (2013) 1–9.
- [8] M. Cutkosky, S. Kim, Design and fabrication of multi-material structures for bioinspired robots, *Phil. Trans. R. Soc. A* 367 (1894) (2009) 1799–1813.
- [9] D. Schmidt, K. Berns, Climbing robots for maintenance and inspections of vertical structures—A survey of design aspects and technologies, *Robot. Auton. Syst.* 61 (12) (2013) 1288–1305.
- [10] M. Murphy, C. Kute, Y. Mengüç, M. Sitti, Waalbot II: Adhesion recovery and improved performance of a climbing robot using fibrillar adhesives, *Int. J. Robot. Res.* 30 (1) (2010) 118–133.
- [11] K. Daltorio, T. Wei, A. Horschler, L. Southard, G. Wile, R. Quinn, S. Gorb, R. Ritzmann, Mini-Whegs TM climbs steep surfaces using insect-inspired attachment mechanisms, *Int. J. Robot. Res.* 28 (2) (2009) 285–302.
- [12] M. Henrey, A. Ahmed, P. Boscariol, L. Shannon, C. Menon, Abigaille-III: A versatile bioinspired hexapod for scaling smooth vertical surfaces, *J. Bion. Eng.* 11 (1) (2014) 1–17.
- [13] Y. Li, A. Ahmed, D. Sameoto, C. Menon, Abigaille II: toward the development of a spider-inspired climbing robot, *Robotica* 30 (01) (2012) 79–89.
- [14] R. Vidoni, A. Gasparetto, Efficient force distribution and leg posture for a bio-inspired spider robot, *Robot. Auton. Syst.* 59 (2) (2011) 142–150.
- [15] G. Lee, H. Kim, K. Seo, J. Kim, M. Sitti, T. Seo, Series of multilinked caterpillar track-type climbing robots, *J. Field Robotics* 33 (6) (2015) 737–750.
- [16] B. He, Z. Wang, M. Li, K. Wang, R. Shen, S. Hu, Wet adhesion inspired bionic climbing robot, *IEEE/ASME Trans. Mechatronics* 19 (1) (2014) 312–320.
- [17] Z. Yu, Structure design of bionic gecko's toe and the adhesive locomotion performance test, *J. Mech. Eng.* 47 (21) (2011) 7–12.
- [18] C. Guo, J. Sun, Y. Ge, W. Wang, D. Wang, Z. Dai, Biomechanism of adhesion in gecko setae, *Sci. Sin. Vitae* 42 (2) (2012) 135–142.
- [19] T. Wang, C. Meng, S. Guan, B. Pei, Structure design of gecko robot with compliant shank, *J. Mech. Eng.* 45 (10) (2009) 1–7.
- [20] Y. Gao, W. Chen, Z. Lu, J. Liu, Bionic mechanism and locomotion control for a cockroach robot, *J. Mech. Eng.* 46 (13) (2012) 91–99.
- [21] M. Spenko, G. Haynes, J. Saunders, M. Cutkosky, A. Rizzi, R. Full, D. Koditschek, Biologically inspired climbing with a hexapedal robot, *J. Field Robotics* 25 (4–5) (2008) 223–242.
- [22] G. Lynch, J. Clark, P. Lin, D. Koditschek, A bioinspired dynamical vertical climbing robot, *Int. J. Robot. Res.* 31 (8) (2012) 974–996.
- [23] W. Provancher, S. Jensen-Segal, M. Fehlberg, ROCR: An energy-efficient dynamic wall-climbing robot, *IEEE/ASME Trans. Mechatronics* 16 (5) (2011) 897–906.
- [24] T. Lam, Y. Xu, Motion planning for tree climbing with inchworm-like robots, *J. Field Robotics* 30 (1) (2013) 87–101.

- [25] A. Asbeck, S. Kim, M. Cutkosky, W. Provancher, M. Lanzetta, Scaling hard vertical surfaces with compliant microspine arrays, *Int. J. Robot. Res.* 25 (12) (2006) 1165–1179.
- [26] A. Sintov, T. Avramovich, A. Shapiro, Design and motion planning of an autonomous climbing robot with claws, *Robot. Auton. Syst.* 59 (11) (2011) 1008–1019.
- [27] A. Parness, M. Frost, N. Thatte, J. King, K. Witkoe, M. Nevarez, M. Garrett, H. Aghazarian, B. Kennedy, Gravity-independent rock-climbing robot and a sample acquisition tool with microspine grippers, *J. Field Robotics* 30 (6) (2013) 897–915.
- [28] X. Guan, H. Zhang, Development of claw-inspired foot structure for wall-climbing robot, *Mech. Electr. Eng. Mag.* 26 (2) (2009) 1–4.
- [29] Y. Liu, S. Sun, X. Wu, T. Mei, A wheeled wall-climbing robot with bio-inspired spine mechanisms, *J. Bion. Eng.* 12 (1) (2015) 17–28.
- [30] L. Jiang, Y. Guan, C. Cai, H. Zhu, Gait analysis of a novel biomimetic climbing robot, *J. Mech. Eng.* 46 (15) (2010) 17–22.
- [31] Y. Guan, H. Zhu, W. Wu, X. Zhou, L. Jiang, C. Cai, L. Zhang, H. Zhang, A modular biped wall-climbing robot with high mobility and manipulating function, *IEEE/ASME Trans. Mechatronics* 18 (6) (2013) 1787–1798.
- [32] S. Wang, H. Jiang, M.R. Cutkosky, A palm for a rock climbing robot based on dense arrays of micro-spines, in: 2016 IEEE/RSJ International Conference on Intelligent Robots and Systems (IROS), Daejeon, 2016, pp. 52–59.
- [33] K. Carpenter, N. Wiltse, A. Parness, Rotary microspine rough surface mobility, *IEEE/ASME Trans. Mechatronics* 21 (5) (2016) 2378–2390.
- [34] G. Liu, Y. Liu, X. Wang, X. Wu, T. Mei, Design and experiment of a bioinspired wall-climbing robot using spiny grippers, in: 2016 IEEE International Conference on Mechatronics and Automation, Harbin, 2016, pp. 665–670.
- [35] F. Xu, X. Wang, G. Jiang, Design and analysis of a wall-climbing robot based on a mechanism utilizing hook-like claws, *Int. J. Adv. Robot. Syst.* 9 (3) (2012) 1–12.
- [36] F. Xu, J. Shen, J. Hu, G. Jiang, A rough concrete wall-climbing robot based on grasping claws, *Int. J. Adv. Robot. Syst.* 13 (5) (2016) 1–10.
- [37] F. Xu, B. Wang, J. Shen, J. Hu, G. Jiang, Design and realization of the claw gripper system of a climbing robot, *J. Intell. Robot. Syst.* 89 (2018) 301–317.
- [38] N. Morozovsky, T. Bewley, Stair climbing via successive perching, *IEEE/ASME Trans. Mechatronics* 20 (6) (2015) 2973–2982.
- [39] E. Gadelmawla, M. Koura, T. Maksoud, I. Elewa, H. Soliman, Roughness parameters, *J. Mater. Process. Technol.* 123 (1) (2002) 133–145.



Soft robotics, Field robotics, Biomimetic Robot, Medical machinery, Mechanical design, Mechatronics.

Fengyu Xu received the B.S. degree in mechanical engineering from Changchun University of Technology, Changchun, China, in 2002. And he received his M.S. degree from Hefei University of Technology in 2005 and the Ph.D. degree from Southeast University in 2009. From 2016 to 2017, he was a visiting scholar with Department of Electrical and Computer Engineering, Michigan State University, USA. He was an associate professor of the Automation Engineering of Nanjing University of Posts and Telecommunications. His main academic interest and research fields are:



Fanchang Meng received the B.Eng. degree in department of electrical engineering from Jiangsu University of Technology, Changzhou, China, in 2017. Currently, he is studying for M.S. degree in control engineering at Nanjing University of Posts and Telecommunications. He is the vice chairman of the graduate student association of Nanjing University of Posts and Telecommunications. His main academic interest and research fields are: Soft robotics, Biomimetic Robot.



Quansheng Jiang received his Ph.D. degree in mechanical engineering from Southeast University, China, in 2009. From 2016 to 2017, he was a visiting scholar with Department of Mechanical and Electrical Engineering, The University of South Wales, UK. Currently he is an associate professor at School of Mechanical Engineering, Suzhou University of Science and Technology, China. His research interests include signal processing and detection systems.



Gaoliang Peng received the B.S., M.S., and Ph.D. degrees in mechanical engineering from the Harbin Institute of Technology in 2001, 2003, and 2007, respectively. He worked as a postdoctoral position at the Department of Computer Science, Harbin Institute of Technology. He is currently an Associate Professor and the Director of the Faculty of Mechatronics and Automation. His research interests include CAD/CAM, robotic servo control, and automatic assembly of mobile radar antenna.